CATHODOLUMINESCENCE CHARACTERIZATION OF ZnO/ZnS NANOSTRUCTURES

ANODIZED UNDER HYDRODYNAMIC CONDITIONS

Arturo Sanz-Marco[a,b], Rita Sánchez-Tovar[a], Miguel Montes Bajo[b], Ramón Manuel Fernández-Domene[a], José García-Antón[a*]

[a]*Ingeniería Electroquímica y Corrosión (IEC). Departamento de Ingeniería Química y Nuclear. ETSI Industriales. Universitat Politècnica de València. Camino de Vera s/n, 46022 Valencia, Spain. jgarciaa@iqn.upv.es*

[b]*Instituto de Sistemas Optoelectrónicos y Microtecnología.*

Universidad Politécnica de Madrid, Avda. Complutense 30, 28040 Madrid, Spain

ZnO/ZnS nanostructures were successfully synthesized by a simple electrochemical anodization of zinc in a glycerol based electrolyte containing sulfide-ammonium fluoride. The influence of different hydrodynamic conditions and anodization potentials during anodization on the morphological and electronic properties of the obtained ZnO/ZnS nanostructures was studied. The anodized samples were characterized using confocal Raman microscopy, X-Ray Diffraction (XRD), Field Emission Scanning Electronic Microscopy (FE-SEM), cathodoluminescence (CL), and photoelectrochemical water splitting tests under standard AM 1.5 conditions. The results showed that hydrodynamic conditions and higher potentials promoted the formation of ZnO/ZnS nanotubes with both higher sulphur content and crystalline defect density, which reduces the near band edge transition value of the materials and improves the photoelectrochemical activity for water splitting. Additionally, the higher photocurrent densities for water splitting were obtained for the samples anodized at the highest anodization potential and under hydrodynamic conditions, increasing in a

71% for the nanostructures anodized at 1000 rpm when the anodization potential changes from 20 to 40V.

Keywords: anodization, cathodoluminescence, photocatalyst, water splitting, ZnO/ZnS nanostructure.

1. Introduction.

In recent years, the use of semiconductors as photocatalysts has gained prominence due to the economic and environmental advantages of this technology [1]. Since Fujishima and Honda used TiO_2 as a photocatalyst for water splitting under ultraviolet (UV) radiation [2], a great research effort has been devoted to improve the performance of this material, and also in the search of new materials that could match TiO_2 or even overcome its performance [3-5]. Among these materials, ZnO presents some interesting characteristics: it is also a wide band-gap semiconductor (3.3-3.4 eV) with an exciton binding energy of 60 meV, 10-100 times higher electron mobility than TiO_2 and low cost due to its abundance and its easy synthesis [6-9]. To obtain novel properties from ZnO, several techniques have been studied, like doping with S [6, 10, 11] or the fabrication of ZnO nanostructures [3, 8, 9, 12].

The use of nanostructures as photocatalysts presents different advantages, like a great surface/volume ratio, which increases the active area that absorbs light and interacts with the electrolyte, or quantum confinement effects that may increase the light absorption [3, 5]. Different ZnO/ZnS nanostructures have been synthetized using techniques like sputtering or chemical vapour deposition [6, 13]. However, during the last decade the fabrication of nanostructures by electrochemical anodization has received great attention [14]. Using an electrolyte containing fluoride ions we can

2

obtain a self-assembled nanostructured oxide layer directly from the metal substrate, which permits using the substrate as back contact of the structures [15, 16]. Moreover, ZnO/ZnS nanostructures in a one-step process can be obtained adding sulfide ions to the electrolyte [17].

The goal of the present work is to study in depth the effect of hydrodynamic conditions and anodization potential on the morphological, structural, electronic and electrochemical properties of the obtained ZnO/ZnS nanostructures.

2. Experimental procedure.

PTFE coated zinc rods (8 mm diameter, 99.999% purity) were abraded, cleaned and anodized under hydrodynamic conditions in a 2-electrode electrochemical cell with a rotating electrode configuration and a platinum foil (1 cm^2) as a counter electrode. In a previous work [18], we found the optimum electrolyte was a freshly prepared glycerol/water (60:40 vol%) media with 0.025 M NH$_4$F and 0.2 M Na$_2$S. Prior to the anodization process, the exposed area of the zinc rods (0.5 cm^2) was abraded with silicon carbide grinding paper (down to number 4000) until we obtained a mirror finish. Then, the samples were introduced in a sonic bath in ethanol for 2 min and dried in a N$_2$ stream. Three different values of anodization potential were studied (20, 30 and 40 V), increasing the potential at a rate of 200 mVs^{-1} and keeping the end potential for 1 hour at four different rotation speeds: 0, 1000, 2000 and 3000 rpm, respectively. The current densities vs. time were registered during anodization.

After anodization, the nanostructures were annealed to improve the crystallinity. Annealing was performed in a furnace at 375 °C (heating up at a rate of 30 °C s^{-1}) in argon atmosphere for 4 hours. In order to evaluate the possible structure changes, the

samples were examined by confocal Raman microscopy (Witec Raman microscope) and X-Ray Diffraction (XRD) (Schimadzu XRD-700) before and after the thermal treatment. For the confocal Raman microscopy measurements, the samples were illuminated with a 632 nm, 420 mW neon laser.

For morphological characterization, a field emission scanning electron microscope (FE-SEM) was used. In addition, to evaluate the optical properties of the samples at different depths, cathodoluminescence (CL) assays were carried out with different acceleration voltage values. The used assembly was a cathodoluminescence detector (Gatan MonoCL4) mounted on a SEM (FEI model Inspect F50).

The photoelectrochemical water splitting of the nanostructures was evaluated using a 3-electrode configuration, with a saturated Ag/AgCl (3 M KCl) as reference electrode, a platinum tip as counter electrode and the nanostructure (with an effective area exposed to the electrolyte of 0.26 cm^2) as working electrode. A mixture of 0.24 M Na_2S and 0.35 M Na_2SO_3, which was previously degasified using nitrogen was used as electrolyte under simulated sunlight conditions AM 1.5 (100 mWcm^{-2}). Photocurrent transients as a function of the applied potential were recorded by chopped light irradiation (60 s in the darkness and 20 s illumination) while scanning the applied potential from -1.0 $V_{Ag/AgCl}$ to 1.2 $V_{Ag/AgCl}$ with a scan rate of 2 mVs^{-1}.

Fig. S1 shows a general scheme of the synthesis and characterization of the nanostructures explained in detail in this section.

3. Results and discussion.

In this section, the results obtained for the characterization of the nanostructures synthetized by electrochemical anodization are discussed. During the electrochemical anodization of the samples a constant voltage was applied for a period of time and current density values were recorded. The trend of the current density was to decrease with time until it stabilises. The current density decrease is associated with a ZnS precursor layer and an oxide layer formation (see supplementary material and Fig. S2 for further information).

3.1. Crystalline structure characterization.

In order to check the crystalline structure of the nanostructures, XRD assays were performed. Fig. 1 shows representative XRD spectra obtained from the sample anodized under 30 V and 2000 rpm. In the obtained XRD spectra we can appreciate the presence of ZnO and ZnS characteristic peaks, which demonstrates the presence of both species in the sample [17]. The peak at 25° corresponds to ZnS phase with the (002) orientation [17]. The peaks located at 36° and 70° are due to the refraction produced by the polycrystalline Zn substrate [17]. The high intensity of the peak centred at 36° is characteristic of the wurtzite ZnO phase, with (101) orientation [19], which is the most abundant phase of the sample. Another ZnO characteristic peak is the one roughly centred at 34°, corresponding to the (002) orientation [20]. The peaks at 32°, 56° and 67° correspond to the wurtzite ZnS phase with (101), (112) and (104) orientation, respectively [21]. Additionally, the peaks at 48° and 63°are related, the former, with the ZnS phase with (110) orientation and the ZnO phase with (102) orientation, and the latter, with the ZnO phase with (103) orientation [17, 19, 20].

Additional characterization was performed with a Raman confocal miscroscope for the as anodized and annealed nanostructures. The Raman spectra of the as-anodized samples show several characteristic ZnO and ZnS peaks. However, after the thermal treatment, a broad background signal due to photoluminescence associated with oxygen vacancies appears in the Raman spectra (see supplementary material and Fig. S3 for further information).

3.2.   Morphological characterization with FE-SEM.

Fig. 2 shows representative surface and cross-sectional FE-SEM images of the ZnO/ZnS nanostructures obtained under different anodization potentials and hydrodynamic conditions. In previous studies it was demonstrated that the use of an aqueous electrolyte containing both sulfide and fluoride ions for Zn anodization produces a compact ZnS layer, under which ZnO/ZnS nanostructures are formed [17, 18]. Fig. 2.a shows the rough surface of the ZnS top layer obtained under stagnant conditions and 20 V. In this case, the anodization of zinc is not homogeneous, due to the formation of bubbles at the anode surface, leading to the formation of precipitates. If anodization takes place under flowing conditions (Fig. 2.b and 2.c), a smooth ZnS top layer is obtained. It is important to point out that the morphology of the ZnO/ZnS layer evolves from a porous sponge morphology (Fig. 2.b) to a porous tubular morphology (Fig. 2.c) as rotation speed is increased. This change in morphology continues as the anodization potential increases. In Fig. 2.d, a porous tubular morphology can be observed for the sample anodized under flowing conditions and 30 V. For higher anodization potential (40 V), the same tubular morphology is obtained even in

stagnant conditions (Fig.2.e). The growing speed of the oxide nanostructures depends on the anodization potential, i.e. nanostructures grow faster at higher anodization potentials [14, 16]. This increase of the growing speed involves lower oxide dissolution, and consequently, a tubular morphology. Another effect of the higher growing speed is that longer nanostructures are obtained. In fact, we measured the length of the obtained nanostructures, obtaining values between ≈360-600 nm at 20 V, ≈800-1100 nm at 30 V and ≈1100-1400 nm at 40 V. Longer nanostructures have more surface/volume relation, increasing interaction with light and the electrolyte, and consequently, improving the photocatalytic activity of the samples.

3.3. Study of CL emission.

CL tests were carried out to study the influence of the anodization parameters on the electronic properties of the nanostructures and the distribution and density of defects throughout the nanostructures. Different parameters were calculated from the CL obtained spectra at several acceleration voltages (5, 10, 20 and 30 kV). Fig. 3 shows an example of a CL spectrum where the studied parameters are indicated. The first peak in the spectrum corresponds to the defect emission band (DEF) [22], whose centre at the x axe gives information on the dominant defect. Moreover, the centre of the second peak at the x axe corresponds to the near band edge (NBE) emission [12, 22, 23], which gives information about the composition of the material. The integrated area of each peak (I_{DEF} and I_{NBE}, respectively) and the ratio I_{DEF}/I_{NBE} can be used to compare the defect densities of the obtained nanostructures.

Table 1 shows the obtained values of the NBE transition energy at an acceleration voltage of 30 kV depending on the anodization conditions. The NBE values were

calculated from the second peak of the CL spectra shown in Fig. 3. It can be observed that the NBE energy decreases as the anodization potential and the rotation speed increase, reaching the minimum value when anodization is carried out at 40 V and hydrodynamic conditions. The lower values of NBE suppose the absorption of a higher fraction of the solar spectrum, and consequently, a better performance of the material as photocatalyst. From NBE values, the sulphur content of the ternary $ZnO_{1-x}S_x$ can be approximated following the Vegard's law as [24]:

$$Eg^{ZnO_{1-x}S_x} = Eg^{ZnO}(1-x) + Eg^{ZnS}x - b(1-x)x \qquad (1)$$

Where $Eg^{ZnO_{1-x}S_x}$ is the value of the obtained NBE transition plus the exciton energy (60 meV) [7, 24], Eg^{ZnO} is the value of the band gap of ZnO (3.37 eV) [7, 24], Eg^{ZnS} is the value of the bandgap of ZnS (3.6 eV) [24], x is the S content and b is the bowing parameter, which is 3.5 eV for $ZnO_{1-x}S_x$ [24]. Table 1 also shows the S content (in %) versus the anodization conditions, reaching the maximum S content for the samples with lower NBE transition, which are the samples anodized at 40 V and under hydrodynamic conditions. The higher growing speed of the nanostructures formation due to higher potential and rotation speed favours the interaction of the oxide with the electrolyte, increasing the oxygen substitution by sulphur in the obtained nanostructures, following the next chemical reaction [8] and, consequently, reducing the value of the NBE transition:
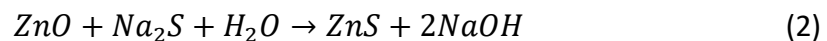
$$ZnO + Na_2S + H_2O \rightarrow ZnS + 2NaOH \qquad (2)$$

Fig. 4 shows the I_{DEF}/I_{NBE} ratio values at 30 kV for the different anodization potentials at the studied rotation speeds.

8

It can be observed in Fig. 4 that the highest defect densities are obtained for the nanostructures anodized at 2000 rpm. At this condition, the interaction between the surface of the zinc rod and the electrolyte during anodization reaches its optimum; therefore, the higher oxygen substitution leads to a higher defect concentration. On the other hand, for the nanostructures anodized under stagnant conditions and 1000 rpm, the ZnS precursor layer is not properly developed, avoiding the correct formation of the samples and, consequently, the defect density values are lower. When the rotation speed is increased to 3000 rpm, the optimum regime is surpassed and the defect concentration is reduced. As the anodization potential is increased, the ion movement is faster [25]. Consequently, the growing speed of the nanostructures formation is higher and the defect density too. This is the reason why, in general, the I_{DEF}/I_{NBE} ratio values are higher as the anodization potential increases.

On the other hand, the centre of the defect band emission (DEF in Fig. 3) is shifted to lower or higher energies depending on the energy emission of the main defect. If we represent this energy versus the acceleration voltage (Fig. 5), the different defects found throughout the depth of the nanostructures can be studied. In Fig. 5.a the defect band emission centre has values between 2.43 and 2.48 eV for every sample, except for the ones obtained at 5 kV of acceleration voltage. These values are typical of the oxygen vacancy (V_O) [22]. The values obtained at 5 kV are shifted to lower energy values due to a higher concentration of oxygen interstitial (I_O) defect, whose emission energy is between 1.9 and 2.1 eV [26]. In this situation, the surface of the material is the most exposed part to the electrolyte, so the oxygen substitution by sulphur in the material is higher in the surface (Eq. 2). These oxygen ions are stuck in the material, creating I_O defects. When the samples were anodized at 30 V (Fig. 5.b),

and under stagnant conditions, the emission centre is ≈2.45 eV for all the acceleration voltages. That is, in stagnant conditions, the ZnS precursor layer reduces the interaction between the nanostructures and the electrolyte. Therefore, the samples anodized under hydrodynamic conditions present the characteristic shift of energy due to the presence of I_O defects. However, at this potential (30V) this defect is also present in deeper zones of the samples. The higher growing speed of the nanostructures formation increases the interaction with the electrolyte at higher depths, and consequently, the generation of I_O defects. In Fig. 5.c this tendency is also observed, that is, a higher concentration of I_O reaches deeper zones, as the interaction with the electrolyte is even stronger.

To sum up, two important tendencies can be observed in Fig. 4 and Fig. 5: as the anodization potential is increased, first, the growing speed of the nanostructures formation is higher, increasing the defect density throughout the sample and second, the interaction with the electrolyte is higher, enhancing the formation of I_O defects in deeper zones of the samples.

3.4.   Photoelectrochemical characterization.

The ZnO/ZnS nanostructures were evaluated as photoanodes in a degasified solution of 0.24 M Na_2S and 0.35 M Na_2SO_3, since it was found to be the most appropriate solution [18]. Fig. 6 shows the photocurrent transient vs. potential curves obtained under simulated sunlight AM 1.5 conditions for the different anodization potentials at the studied rotation speeds.

Fig. 6.a shows that, in general, the samples anodized at 20 V are not photocorrosion resistant due to their high dark current values. This fact could be associated with the ZnS precursor layer that is not properly formed at 20V (see Fig. 2), which affects both the nanostructure formation and the photocorrosion resistance of the ZnS precursor layer. On the other hand, Figs. 6.b and 6.c show that the samples anodized at higher potentials (30 and 40V) are photocorrosion resistant. For instance, from -0.4 to 0.2 $V_{Ag/AgCl,}$ nanostructures formed at these potentials present good stability, that is, dark current values close to zero and high photocurrent densities (see Figs. 6.b and 6.c). Additionally, the photocurrent densities for the nanostructures anodized at 30 and 40V increase with the rotation speed. In fact, the morphology of the nanostructures anodized at 30 V presented more tubular aspect as the rotation speed was increased and the ones anodized at 40V, showed nanotubular morphology even when anodization was performed without rotating the electrode. This morphology facilitates the charge separation [3, 8, 27-29], and consequently, the photocatalytic response. This is in agreement with the decrease of the NBE transition value as the rotation speed is increased (Table 1), which means that the absorbed fraction of solar spectra is higher.

In particular, the optimal conditions were obtained for the samples anodized at 40V and at 1000 rpm, where the photocurrent density for photoelectrochemical water splitting increases in a 71% in comparison to the photocurrent density achieved for the nanostructure anodized at 20V and 1000 rpm. At these optimal conditions, the nanostructure possesses the highest defect density (see Fig. 4) and presence of I_o defects is significant (Fig. 5.c). The higher density of I_o defects in this sample increases the presence of available additional energetic states, enabling the absorption of light and the creation of electron-hole pairs. In addition, the value of the NBE transition of this nanostructure is one of the lowest (Table 1). Therefore, both the higher density of I_o and the lower NBE energy value, increase the absorption of light and improve the photocatalytic performance of the samples.

4. Conclusions.

In the present work the influence of two anodization parameters were studied for the formation of ZnO/ZnS nanostructures: the anodization potential and the rotation speed during the electrochemical procedure.

The presence of ZnO and ZnS was confirmed by XRD, being wurtzite the predominant phase.

The morphology of the obtained nanostructures is strongly dependent on the anodization potential and the hydrodynamic condition during anodization. Morphology changes from nanosponge to porous nanotubular arrays as the anodization potential and rotation speed increase.

According to the CL measurements, the main defects found in the samples are the oxygen vacancies and interstitial oxygens. Under stagnant conditions, the major defect

is the oxygen vacancy, but as the rotation speed is increased, the density of the interstitial oxygen also increases. The NBE transition value is reduced as the anodization potentials and hydrodynamic conditions are increased.

The ZnO/ZnS nanostructures succeed as photocatalyst for photoelectrochemical water splitting in polysulfide aqueous solutions. The best results were obtained as the anodization potential increased and under hydrodynamic conditions, for the samples with lower values of the NBE transition and higher defect densities. In particular, the optimal conditions were obtained for the samples anodized at 40V and at 1000 rpm, where the photocurrent density for photoelectrochemical water splitting increased in a 100% with respect to the one obtained for the sample anodized at 20V and at 0 rpm, and in a 71% in comparison to the photocurrent density achieved for the nanostructure anodized at 20V and 1000 rpm.

References

[1] A.A. Ismail, D.W. Bahnemann, Photochemical splitting of water for hydrogen production by photocatalysis: A review, *Solar Energy Materials & Solar Cells*, 2014, 128, 85-101.

[2]. A. Fujishima, K. Honda, Electrochemical evidence for the mechanism of the primary stage of photosynthesis Bull, *Chem. Soc. Jpn*, 1971, 44, 1148–1150.

[3] S. Chen, S.S. Thind, A. Chen, Nanostructured materials for water splitting - state of the art and future needs: A mini-review, *Electrochemistry Communications*, 2016, 63, 10-17.

[4] H. Ahmad, S.K. Kamarudin, L.J. Minggu, M. Kassim, Hydrogen from photo-catalytic water splitting process: A review, *Renewable and Sustainable Energy Reviews,* 2015, 43, 599-610.

[5] J. Zhu, M. Zäch, Nanostructured materials for photocatalytic hydrogen production, *Current Opinion in Colloid & Interface Science*, 2009, 14, 260-269.

[6] V. Khomyak, I. Shtepliuk, V. Khranovskyy, R. Yakimova, Band-gap engineering of $ZnO_{1-x}S_x$ films grown by rf magnetron sputtering of ZnS target, *Vacuum*, 2015, 121, 120-124.

[7] N. Samir, D.S. Eissa, N.K. Allam, Self-assembled growth of vertically aligned ZnO nanorods for light sensing applications, *Materials Letters*, 2014, 137, 45-48.

[8] A. Kushwaha, M. Aslam, ZnS shielded ZnO nanowire photoanodes for efficient water splitting, *Electrochimica Acta*, 2014, 130, 222-231.

[9] S.A. Mahmouda, O.A. Fouad, Synthesis and application of zinc/tin oxide nanostructures in photocatalysis and dye sensitized solar cells, *Solar Energy Materials & Solar Cells*, 2015, 136, 38-43.

[10] X.H. Wang, S. Liu, P. Chang, Y. Tang, Synthesis of sulfur-doped ZnO nanowires by electrochemical deposition, *Materials Science in Semiconductor Processing*, 2007, 10, 241-245.

[11] A.B. Patil, K.R. Patil, S.K. Pardeshi, Ecofriendly synthesis and solar photocatalytic activity of S-doped ZnO, *Journal of Hazardous Materials*, 2010, 183, 315-323.

[12] S. He, M. Zheng, L. Yao, X. Yuan, M. Li, L. Ma, W. Shen, Preparation and properties of ZnO nanostructures by electrochemical anodization method, *Applied Surface Science*, 2010, 256, 2557-2562.

[13] E.S. Babu, S.Kim, J.H. Song, S.K. Hong, Effects of growth pressure on morphology of ZnO nanostructures by chemical vapour transport, *Chemical Physics Letters*, 2016, 658, 182-187.

[14] X. Zhou, N. Truong Nguyen, S. Özkan, P. Schmuki, Anodic TiO_2 nanotube layers:Why does self-organized growth occur — A mini review, *Electrochemistry Communications*, 2014, 46, 157-162.

[15] S.J. Kim, J. Lee, J. Choi, Understanding of anodization of zinc in an electrolyte containing fluoride ions, *Electrochimica Acta*, 2008, 53, 7941-7945.

[16] D. Khudhair, A. Bhatti, Y. Li, H. Amani Hamedani, H. Garmestani, P. Hodgson, S. Nahavandi, Anodization parameters influencing the morphology and electrical

properties of TiO2 nanotubes for living cell interfacing and investigations, *Materials Science and Engineering C*, 2016, 59, 1125-1142.

[17] N.K. Shrestha, K. Lee, R. Hahn, P. Schmuki, Anodic growth of hierarchically structured nanotubular ZnO architectures on zinc surfaces using a sulfide based electrolyte, *Electrochemistry Communications*, 2013, 34, 9-13.

[18] R. Sánchez-Tovar, R. M. Fernández-Domene, M. T. Montañés, A. Sanz-Marco, J. Garcia-Antón, ZnO/ZnS heterostructures for hydrogen production by photoelectrochemical water splitting, *RSC Advances*, 2016, 6, 30425.

[19] M. M. H. Farooqi, R. K. Srivastava. Structural, optical and photoconductivity study of ZnO nanoparticles synthesized by annealing of ZnS nanoparticles. Journal of Alloys and Compounds, 2017, 691, 275-286.

[20] P.C. Patel, S. Ghosh, P.C. Srivastava. Structural, magnetic and optical properties of ZnO nanostructures converted from ZnS nanoparticles. Materials Research Bulletin, 2016, 81, 85-89.

[21] P. Roy, S.Berger. P. Schmuki. TiO2 nanotubes: synthesis and applications. Angew. Chem. Int. Ed., 2011, 50, 2909-2939.

[22] R. Yousefi, B. Kamaluddin. The effects of annealing temperature on structural and optical properties of S-doped ZnO nanobelts. Solid State Sciences, 2010, 12, 252-256.

[23] J. Zhao, L. Qin, L. Zhang. Fabrication of ZnS/ZnO hierarchical nanostructures by two-step vapour phase method. Materials Research Bulletin, 2009, 44, 1003-1008.

[24] V. Khomyak, I. Shtepliuk, V. Khranovskyy, R. Yakimova. Band-gap engineering of $ZnO_{1-x}S_x$ films grown by rf magnetron sputtering of ZnS target. Vacuum, 2015, 121, 120-124.

[25] D. Khudhair, A. Bhatti, Y. Li, H. Amani Hamedani, H. Garmestani, P. Hodgson, S. Nahavandi. Anodization parameters influencing the morphology and electrical properties of TiO2 nanotubes for living cell interfacing and investigations. Materials Science and Engineering C, 2016, 59, 1125-1142.

[26] H. Zhang, R. Xie, T. Sekiguchi, X. Ma, D. Yang. Cathodoluminescence and its mapping of flower-like ZnO, ZnO/ZnS core–shell and tube-like ZnS nanostructures. Materials Research Bulletin, 2007, 42, 1286-1292.

[27] J. Zhu y M. Zäch. Nanostructured materials for photocatalytic hydrogen production. Current Opinion in Colloid & Interface Science, 2009, 14, 260-269.

[28] Y. Kim, J. Park, S. Kim, D. W. Park, J. Choi. Fabrication of hierarchical ZnO nanostructures for dye-sensitized solar cells. Electrochimica Acta, 2012, 78, 417-421.

[29] S. Sreekantan, L. R. Gee, Z. Lockman. Room temperature anodic deposition and shape control of one-dimensional nanostructured zinc oxide. Journal of Alloys and Compounds, 2009, 476, 513-518.
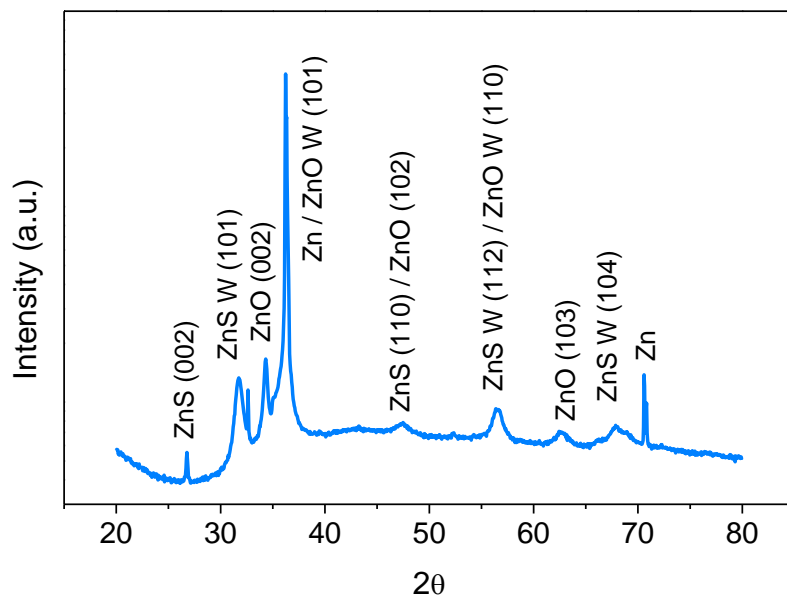
Figure 1. XRD spectra of the sample anodized at 30 V and 2000 rpm after the thermal treatment at 375°C in argon atmosphere for 4 hours. W means wurtzite phase.
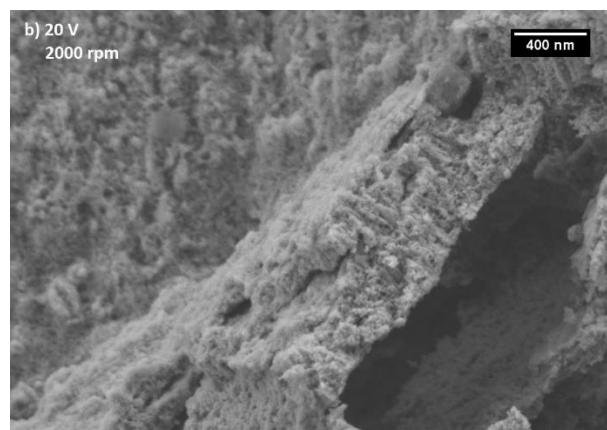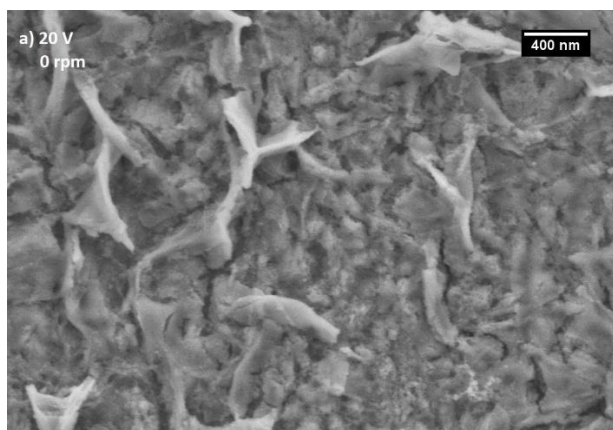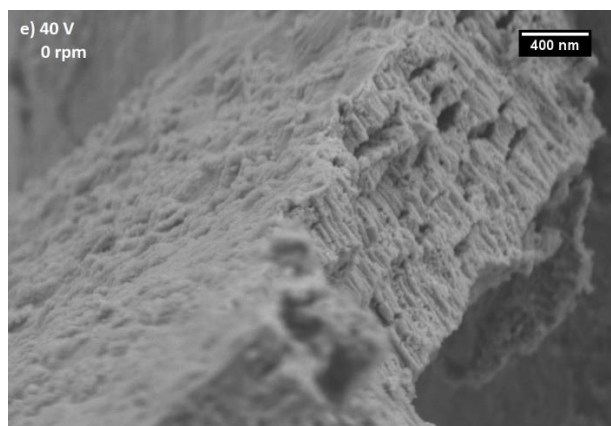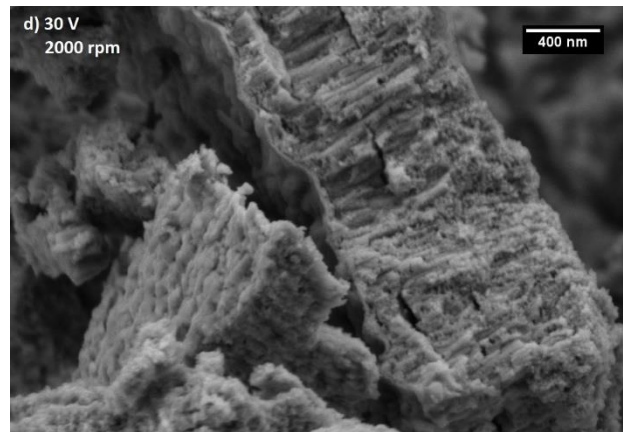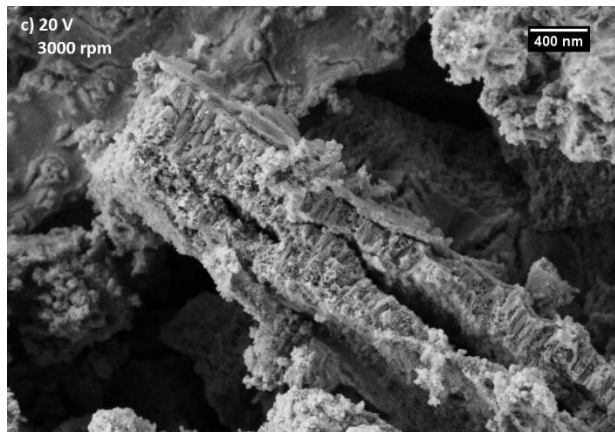
Figure 2. FE-SEM images of the ZnO/ZnS nanostructures anodized at 20 V under stagnant conditions (a), at 2000 rpm (b) and 3000 rpm (c) at 30V and at 2000 rpm and (d) at 40 V and under stagnant conditions (e).
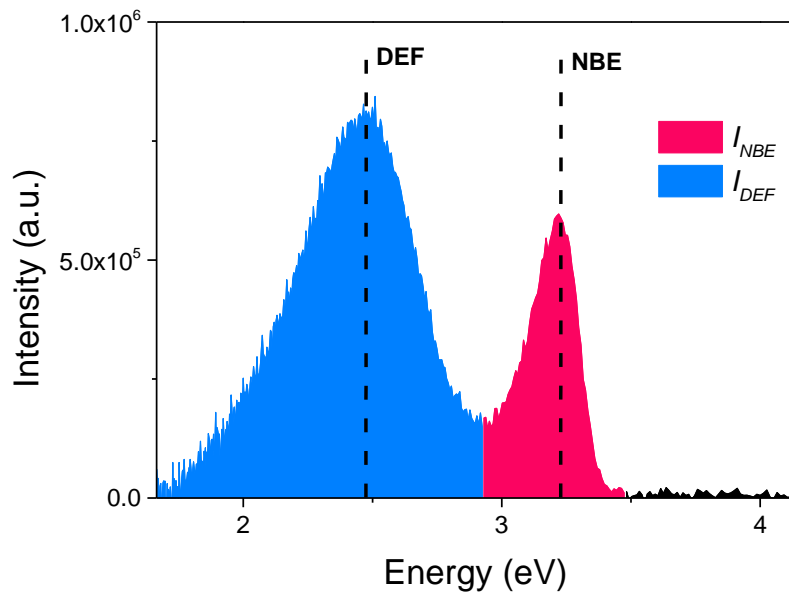
Figure 3. Example of an obtained CL spectrum at 30 kV of a nanostructure anodized at 20V and 0 rpm, with the defect band emission centre (DEF), the near band edge energy transition (NBE), the integrated area of the NBE peak (I_{NBE}) and the integrated area of the defect band (I_{DEF}).
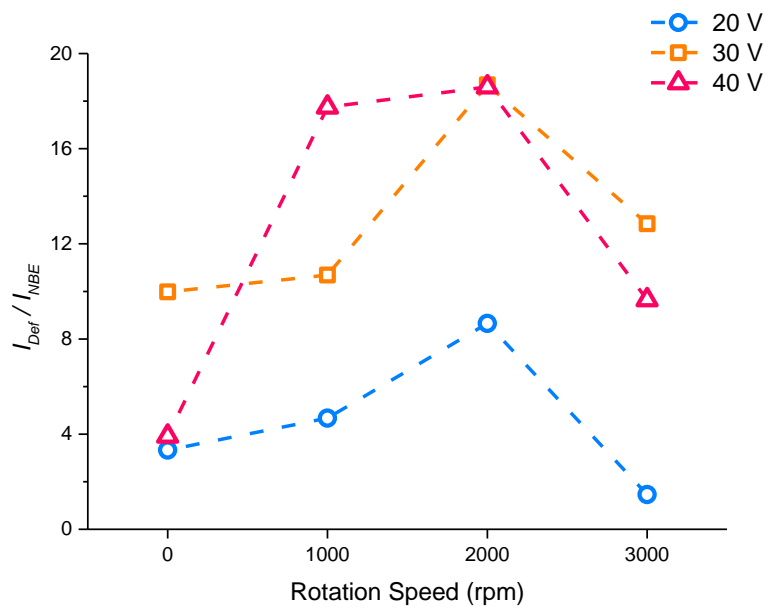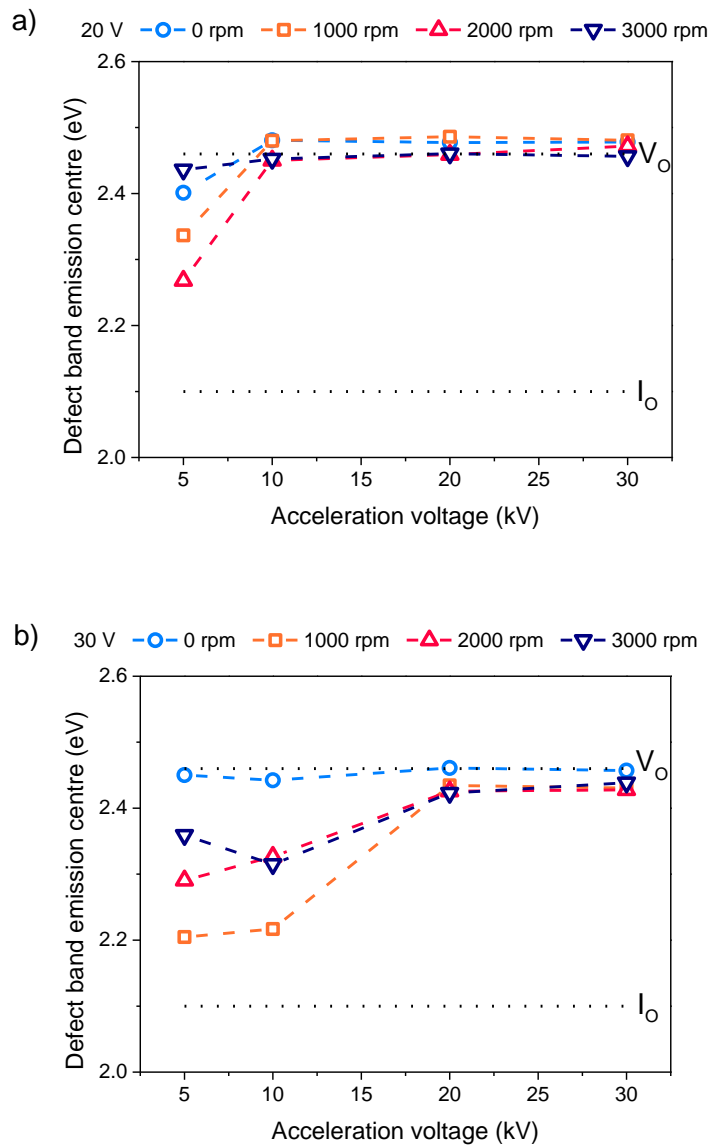
Figure 4. I_{DEF}/I_{NBE} ratio values versus rotation speed of the samples anodized at 20, 30 and 40 V at an acceleration voltage of 30 kV. I_{DEF} and I_{NBE} correspond to the integrated areas of the defect emission band and the near band edge, respectively, and are calculated according to Figure 3.
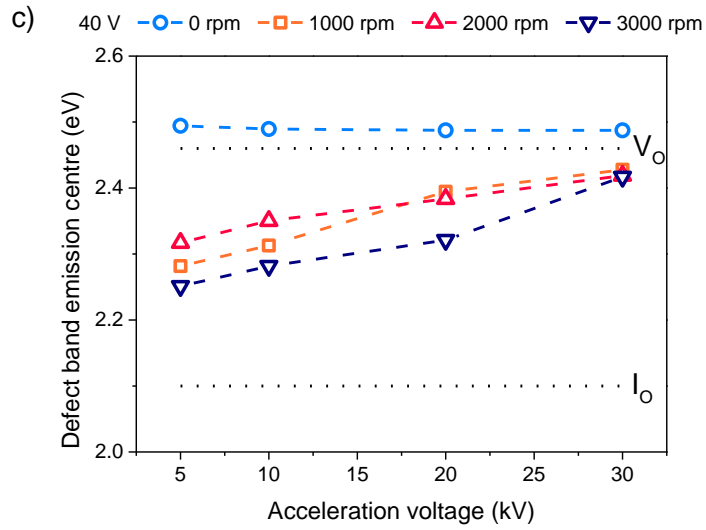
Figure 5. Defect band emission centre against acceleration voltage of the samples anodized under 20 V (a), 30 V (b) and 40 V (c) at the different rotation speeds. V_0 refers to the oxygen vacancy values and I_0 to the oxygen intertitials.
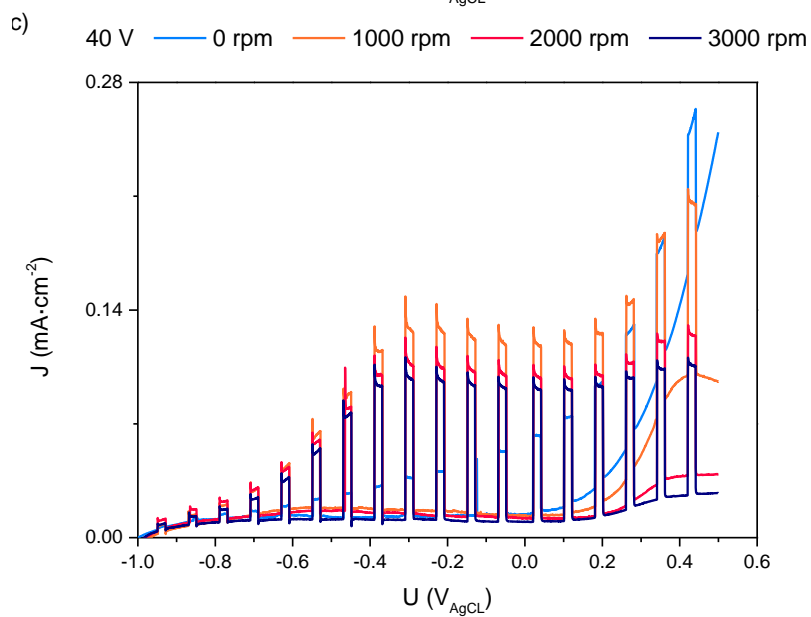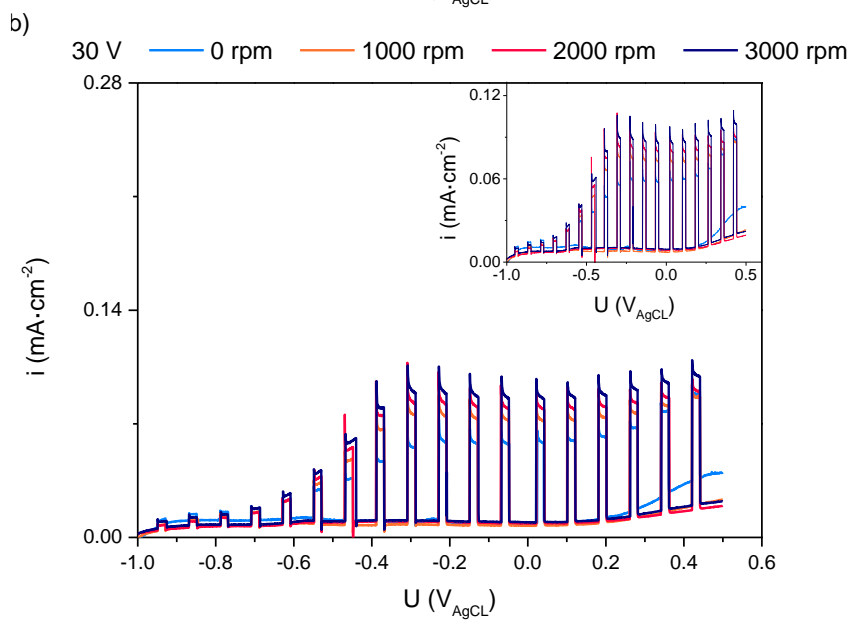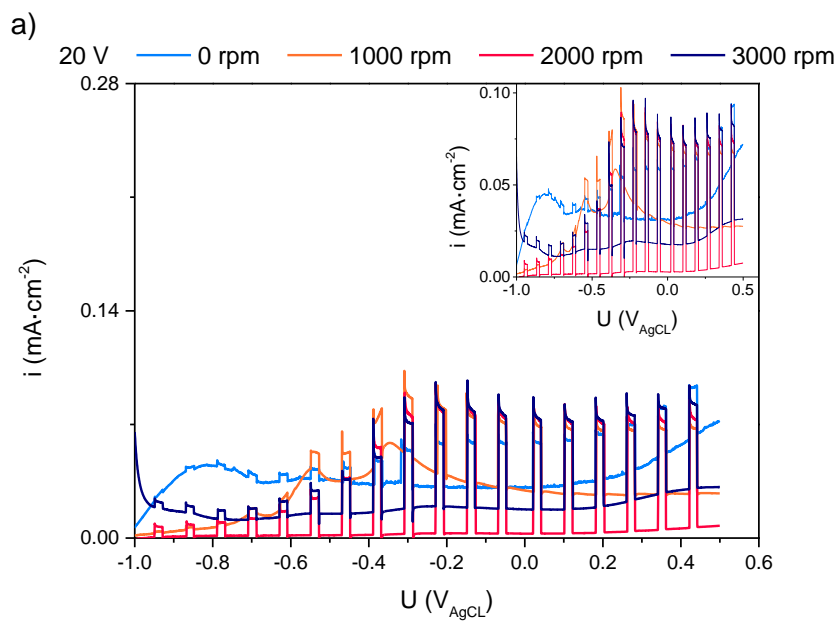
a)

b)

c)

Figure 6. Photocurrent density transients of the different ZnO/ZnS nanostructures anodized at the different rotation speeds under 20 V (a), 30 V (b) and 40 V (c) measured in a 0.24 M Na$_2$S and 0.35 M Na$_2$SO$_3$ solution under AM 1.5 illumination, as a function of the applied potential.

Table 1. Data corresponding to the NBE transition energy and the corresponding S content measured of the samples at an acceleration voltage of 30 kV versus the anodization condition.

Anodization Potential (V)	Hydrodynamic conditions (rpm)	NBE Transition Energy (eV)	Sulphur content (%)
20	0	3.23	2.65
	1000	3.23	2.58
	2000	3.22	2.96
	3000	3.20	3.36
30	0	3.20	3.36
	1000	3.19	3.79
	2000	3.18	4.01
	3000	3.18	4.10
40	0	3.26	1.67
	1000	3.16	4.69
	2000	3.16	4.82
	3000	3.17	4.44